PCCP

Accepted Manuscript

ROYAL SOCIETY OF CHEMISTRY

www.rsc.org/pccp

Journal Name

ARTICLE TYPE

Cite this: DOI: 10.1039/xxxxxxxxxx

Dehydrogenation of Methanol to Formaldehyde Catalyzed by Pristine and Defective Ceria Surfaces†

Ariana Beste*[ab] and Steven H. Overbury[c]

Received Date
Accepted Date

DOI: 10.1039/xxxxxxxxxx

www.rsc.org/journalname

We have explored the dehydrogenation of methoxy on pristine and defective (111), (100), and (110) ceria surfaces with density functional methods. Methanol conversion is used as a probe reaction to understand structure sensitivity of the oxide catalysis. Differences in reaction selectivity have been observed experimentally as a function of crystallographically exposed faces and degree of reduction. We find that the barrier for carbon-hydrogen cleavage in methoxy is similar for the pristine and defective (111), (100), and (110) surfaces. However, there are large differences in the stability of the surface intermediates on the different surfaces. The variations in experimentally observed product selectivities are a consequence of the interplay between barrier controlled bond cleavage and desorption processes. Subtle differences in activation energies for carbon-hydrogen cleavage on the different crystallographic faces of ceria could not be correlated with structural or electronic descriptors.

1 Introduction

Cerium oxide is a technologically important material functioning as a catalyst and a catalyst support, where it enhances the activity of platinum group metals[1,2]. Its characteristic properties are ease of reduction involving the transition from Ce^{4+} to Ce^{3+} and high oxygen mobility. Doping with, for instance Gadolinium or Samarium, increases the oxygen ion conductivity further through vacancy formation. This is exploited in the application of doped ceria as a material for solid oxide fuel cells[1]. Traditionally, cerium oxide has been used in three-way catalysts[3] by the automotive industry to reduce the emission of harmful exhaust gases. More recent utilizations; for instance, as an antioxidant adsorbing reactive species in cell cultures[4] and in vivo[5], have become possible because of the development of advanced synthesis techniques to produce nanostrcutured ceria[6].

In our experimental program we have used CeO_2 single crystal surfaces[7,8] and ceria nanoparticles[9–11] with specific morphologies to explore the role of surface structure upon adsorption and reactions. In these faceted nanoparticles, cubes expose only (100) crystallographic faces, while octahedra show primarily (111) surfaces, and nanorods display a mixture of faces. Reactivity and selectivity in methanol decomposition has been measured as a function of surface structure and catalyst morphology in temperature-programmed and steady-state reactor experiments[7,11]. Dehydrogenation of alcohols has been used as a probe reaction to charac-

[a] *Address, Joint Institute for Computational Sciences, The University of Tennessee, Oak Ridge, TN 37831, USA. Fax: 865-241-4811; Tel: 865-241-3160; E-mail: bestea@ornl.gov*

[b] *Address, Center for Nanophase Materials Sciences, Oak Ridge National Laboratory, Oak Ridge, TN 37831, USA.*

[c] *Address, Chemical Sciences Division, Oak Ridge National Laboratory, Oak Ridge, TN 37831, USA.*

† Electronic Supplementary Information (ESI) available: NEB paths for C-H cleavage and formaldehyde conversion on the pristine and defective (111), (100), and (110) ceria surfaces; energy profiles for methanol conversion to formaldehyde on the pristine (100) surface comparing the relative position of the coadsorbed hydrogen, on the defective (100) surface comparing conversion over a vacancy and next to a vacancy, on the defective (110) surface comparing hydrogen transfer to different neighbouring surface oxygen atoms; plot of methanol adsorption energies versus Ce coordination number; and projected density of state comparing surface oxygen to which hydrogen is transferred and a 4th layer oxygen for methoxy on the pristine and defective (111), (100), and (110) ceria surfaces. See DOI: 10.1039/b000000x/

terize catalytic properties of oxide materials[12,13]. Methanol, the smallest of all alcohols, adsorbs on CeO_2 at low temperature by O-H cleavage to form methoxy and a co-adsorbed hydrogen. But, at higher temperatures the C-H bond of the methyl can be activated leading to dehydrogenation of the molecule. In single crystal[7] as well as reactor experiments[11] differences in reaction selectivity are controlled by the structure and the degree of reduction of the surfaces. Structure dependence in oxides may be linked to acid/base properties of the oxide surface, vacancy formation, reducibility of the oxide surface and geometry of the adsorption site. Site geometry can influence sterics for reactions and cooperativity between acid and base sites. A key question is how these factors combine to control the activation of the α-C-H bond in methanol. Here, we explore this question computationally using density functional theory (DFT). In particular, we want to understand how the adsorption site type, the geometry, the degree of reduction, and the basicity of the hydrogen receiving surface oxygen on the (111), (100), and (110) surfaces influence the C-H bond cleavage, which is the initial step of the dehydrogenation of methoxy on the ceria surface.

DFT has been used in previous work to study the dissociative adsorption of methanol on the (111) surface[14,15]. Recently, Kropp et al. have extended this work to include dehydrogenation up to formaldehyde on the fully oxidized as well as the partially reduced (111) surface[16]. The authors concluded that the reactive sites for methanol oxidation are oxygen vacancies since adsorption in a cerium atop site is not strong enough to prevent desorption of methanol before reaction. However, a commonly disregarded experimental observation is low temperature water desorption in the temperature programmed desorption (TPD) spectra[7,17,18] of methanol over ceria thin films. If the coadsorbed hydrogen is removed as water, methoxy cannot be hydrogenated to desorb from the surface. Therefore, the consequence of low temperature water desorption is both the loss of surface lattice oxygen and the stabilization of methoxy, even for TPD from an initially, fully oxidized surface.

Detailed investigations of the methanol decomposition mechanism on ceria surfaces up to carbon oxides have been undertaken very recently[19,20], although in the latter studies, oxygen vacancies were not considered as reactive sites. Related work on the fully oxidized (110) ceria surface for initial bond breaking in methanol (albeit not methoxy) have been reported[21]. Other relevant work includes the investigation of ceria support effects on methanol oxidation[22], DFT studies on formaldehyde adsorption[23,24] and oxidation[24] on ceria, and the examination of pathways for dehydrogenation and dehydration for methanol's larger homolog, ethanol[25].

In the following, we present computational details, results, and discussion of our study of the α-C-H cleavage in methoxy to form formaldehyde on the (111), (100), and (110) ceria surfaces. This extends previous comparative investigations of the three surfaces[19] to include dehydrogenation of methoxy reacting at oxygen vacancy sites. This is important because even on the fully oxidized surfaces, low temperature water formation removes surface oxygen, which implies oxygen vacancies[7,17] that can trap methoxy. We find that TPD product distributions are a consequence of the interplay between barrier controlled dehydrogenation and desorption processes.

2 Computational Details

All electronic structure calculations are carried out using the projector-augmented wave (PAW) method[26,27] as implemented in the Vienna ab initio simulation package (VASP)[28–31]. The DFT+U method is commonly used to overcome shortcomings of standard gradient-corrected exchange-correlation functional to properly localize electrons in reduced ceria. We refer to an excellent review on computational work on ceria surface chemistry[32]. In particular, we employ the PBE+U[33,34] functional. A value of 5.0 eV for U is optimized to position occupied Ce 4f states about 1.3 eV above the oxygen 2p states in bulk Ce_2O_3[35] and a value close to it (4.5 eV) has been used in recent methanol dehydrogenation studies mentioned above[16,19]. It was observed that a lower value of U (2.0-3.0 eV) results in a better description of the redox chemistry over ceria surfaces[36] and in bulk[37]. Similarly, a low U value was recommended for the calculation of activation barriers[38]. Our work on methanol conversion over ceria[39] also suggests that a value of 3.0 eV agrees better with hybrid functional results[16] for reduction processes. For f-electrons to localize on cerium, a minimum value of 3.0 eV[40] was reported. In our experience, U=3.0 eV is not always sufficient for proper localization, particularly during geometry optimizations. Since electron localization influences the defect structure and vice versa, we use a value of 5.0 eV for the relaxation of vacancy structures, a value of 3.0 eV otherwise. All energies are reported utilizing a value of 3.0 eV for U.

The (111) and the (100) surface cells are constructed by stacking 9 atomic layers while the larger (110) cell only contains 7 atomic layers. While the (111) and the (100) surfaces are oxygen terminated, the top layer of the (110) surface contains cerium and oxygen atoms. To compensate for the nonzero dipole moment normal to the (100) surface, 50% of the top layer oxygen atoms are removed and added to the bottom (forming the ninth atomic layer) in a checker board configuration, which was found to be most stable[41]. The slabs are separated by a vacuum layer of 15 Å. We use a p(2x2) expansion of the surface cells, within which one methanol molecule is dissociatively adsorbed. The partially reduced surfaces are modelled by including a single oxygen vacancy in the top layer of the surface cell. For the (111) surface, we believe that the single oxygen vacancy is a good model at moderate degree of reduction[42]. Vacancy clustering is not expected and the subsurface/surface vacancy distribution is controlled by thermodynamic equilibrium[42]. For the (100) and the (110) surfaces, we follow common practice[43]. Using the p(2x2) expansion, this amounts to a vacancy and methoxy/H coverage of 1.9 nm^{-2}, 1.7 nm^{-2}, and of 1.2 nm^{-2} for the (111), (100), and (110) surface respectively. The cerium site surface concentration is 31.0 nm^{-2}, 26.9 nm^{-2}, and 19.0 nm^{-2} and the vacancy surface concentration as it applies is 7.8 nm^{-2}, 6.7 nm^{-2}, and 4.7 nm^{-2} for the (111), (100), and (110) surface respectively. Removing one surface oxygen results in an oxygen vacancy with two electrons remaining in the surface. These electrons localize in cerium 4f-bands reducing two Ce^{4+} to Ce^{3+} ions that are nearest and next-nearest neigh-

bors to the vacancy on the (111) surface[42]. On the (100) surface these electrons were reported to be located next to the vacancy in the lowest energy solution[43]. However, with our computational set-up, an energetically lower solution is obtained when the Ce^{3+} ions are located nearest and next nearest to the vacancy in the second layer. Similarly, the previously documented lowest energy configuration on the (110) surface[44] does not coincide with the energetically more favourable solution obtained with our computational parameters, where the electrons are situated at the top next-nearest neighbor and second layer nearest neighbor cerium atom to the vacancy. Although, we have not searched for the globally lowest solutions for the location of the Ce^{3+} ions, we use the configurations that we found to be lower as initial structures for adsorbate relaxation. We do not constrain the magnetic moments and the Ce^{3+} location may change during the relaxation. The oxidized and partially reduced ceria surface cells without adsorbate are depicted in Figure 1. Experimental values for desorption energies given in the text are derived from TPD data[7] using Redhead analysis[45]. In the latter analysis, the prefactor accounting for entropic effects and usually assumed to be $1.0*10^{13}s^{-1}$ is calculated using the formula derived in a recent report[46] with the gas phase entropy of formaldehyde of 218.95 $JK^{-1}mol^{-1}$ [47].

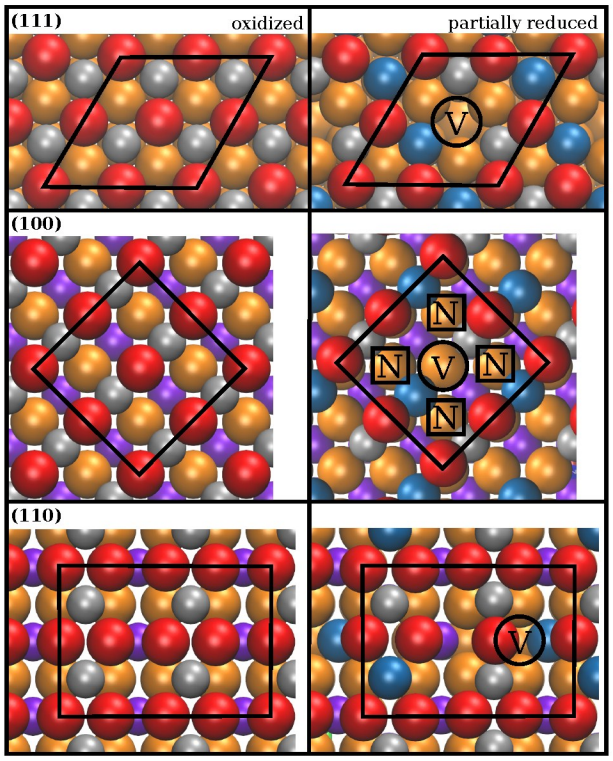

Fig. 1 Top view of surface cells used herein; crystal radii[48] used for rendering of the surfaces; orange - oxygen (general), red - oxygen top layer, purple - cerium (general), silver - cerium second layer for the (111) and (100) surfaces, top layer for the (110) surface, blue - reduced cerium, V indicates vacancy location, N marks adsorption site next to vacancy.

During optimizations of minimum adsorbate structures and reaction paths, the top 6 atomic layers are relaxed for calculations on the (111) and (100) surfaces and the top 5 layers are relaxed for calculations on the (110) surface. The remaining layers are fixed. We employ spin-polarized functionals, an energy cut off of 700 eV, a Γ-centered 3-3-1 Monkhorst-Pack k-point mesh, and dipole corrections perpendicular to the surface. Dispersion corrections are included through the D3 method by Grimme[49]. Minimum energy paths are preoptimized with the nudged elastic band (NEB) method[50] and transition states are located with the climbing image nudged elastic band method[51] (CI-NEB), where we use tools provided by the Henkelman group to set up the input. Transition states are confirmed by frequency analysis. The dissociative adsorption energy is defined as the sum of adsorption energy and dissociation energy. For the case of methanol, it is the energy difference between methoxy and coadsorbed hydrogen on the surface and the sum of methanol and clean surface energy. Formaldehyde adsorption energies are given within the context of methanol conversion; i.e., with reference to two hydrogen adsorbed on the surface. A positive adsorption energy indicates exothermic adsorption.

3 Results and Discussion

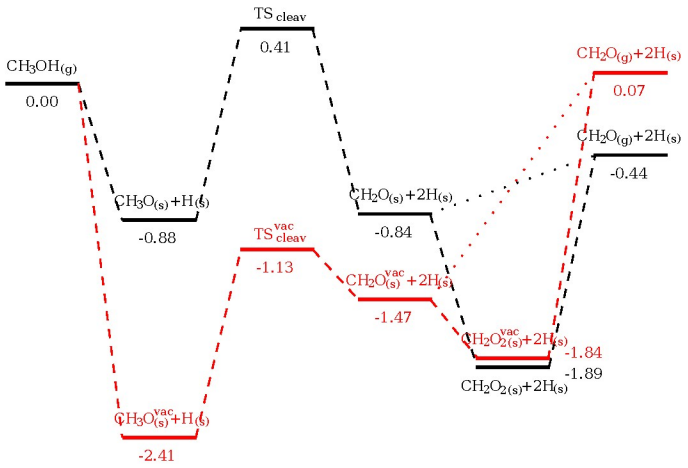

Fig. 2 Energy profile for methanol conversion to formaldehyde on the pristine surface (black lines) and over an oxygen vacancy (red lines) on the (111) ceria surface; energies in eV, subscript (g) indicates gas phase, subscript (s) denotes adsorbed on surface, superscript vac signifies adsorbate in vacancy, TS_{cleav} is the transition state for methoxy C-H cleavage.

We report results for methanol conversion to formaldehyde on pristine ceria surfaces and over vacancy sites for the (111), (100), and (110) crystallographic orientations. While this constitutes complete reaction on the fully oxidized (111) surface in TPD experiments, formaldehyde formation is the initial step of methanol conversion on the reduced (111) as well as oxidized and reduced (100) surfaces, which is followed by further dehydrogenation of formaldehyde[7]. We did not investigate the O-H bond cleavage in methanol, since we calculated a barrier for O-H bond breaking of 0.1 eV on the oxidized (111) surface[39]. We assume that O-H bond cleavage is similarly feasible at low temperature on other surfaces as well, which is supported by experiment[18] and recent work on oxidized surfaces[19]. The corresponding energy profiles are given in Figures 2-4. Table 1 summarizes dissocia-

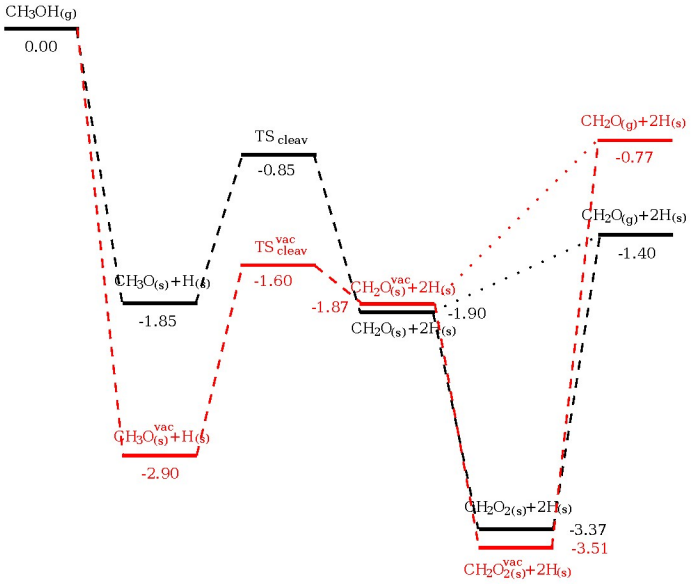

Fig. 3 Energy profile for methanol conversion to formaldehyde on the pristine surface (black lines) and over an oxygen vacancy (red lines) on the (100) ceria surface; energies in eV, subscript (g) indicates gas phase, subscript (s) denotes adsorbed on surface, superscript vac signifies adsorbate in vacancy, TS_{cleav} is the transition state for methoxy C-H cleavage.

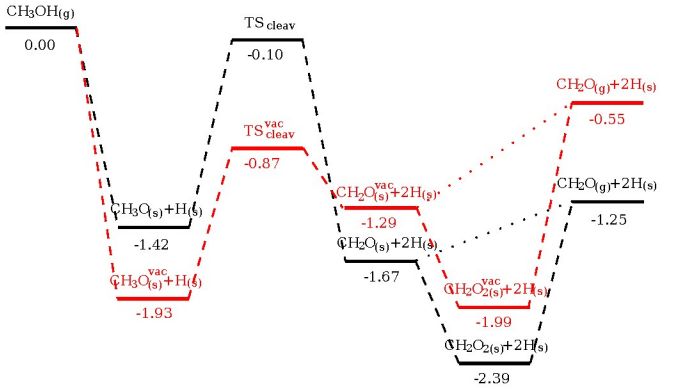

Fig. 4 Energy profile for methanol conversion to formaldehyde on the pristine surface (black lines) and for the energetically lowest path over an oxygen vacancy (red lines) on the (110) ceria surface; energies in eV, subscript (g) indicates gas phase, subscript (s) denotes adsorbed on surface, superscript vac signifies adsorbate in vacancy, TS_{cleav} is the transition state for methoxy C-H cleavage.

tive adsorption energies of methanol, barriers for C-H cleavage, and desorption energies of bidentate formaldehyde. Our results agree well with recent reports on pristine ceria surfaces [19,20] and on the (111) surface [16] with largest differences in the reaction energies for C-H cleavage, which involves reduction of Ce^{4+} to Ce^{3+}. This is due to the overstabilization of Ce^{3+} when high U values are used. For pristine surfaces only and in agreement with us, the activation energy for C-H cleavage on the (100) surface was computed to be lowest in recent work [19] followed by the corresponding barriers on the (111) and (110) surfaces. Slightly lower barriers of a few tenths of an eV computed previously [19], are in line with the higher U value used in that study.

Table 1 Dissociative adsorption energies (sum of adsorption and dissociation energy) of methanol (ΔE_{ads}), activation energies for C-H cleavage in methoxy (ΔE_{act}), and desorption energies of formaldehyde (ΔE_{des}) relative to the surface with two adsorbed hydrogen atoms, lowest energy pathways only; also included is the Ce-methoxy coordination number (CN); experimental values for the (111) and (100) surfaces obtained from TPD spectra [7].

surface	site	CN	ΔE_{ads}	ΔE_{act}	ΔE_{des}	exp
(111)	atop Ce	1	0.88	1.29	1.46	1.91
	vacancy	3	2.41	1.28	1.91	2.19
(100)	lattice O	2	1.85	0.99	1.97	1.91
	vacancy	2	2.90	1.30	2.74	-
(110)	atop Ce	1	1.42	1.32	1.14	N/A
	vacancy	3	1.93	1.06	1.44	N/A

Comparing the energy profiles in Figures 2-4, we observe a qualitative agreement of the conversion to formaldehyde for the different surfaces. While barriers for C-H cleavage are similar regardless of crystallographic orientation and degree of reduction, the biggest differences lie in the adsorption strength of surface intermediates. If a vacancy is present, methoxy binds preferably at the vacancy site, where the missing lattice oxygen is replaced by methoxy oxygen. It was stated recently [20] that the methoxy adsorption strength correlates with its coordination number to surrounding cerium atoms. This was derived from data for both (111) surfaces and the pristine (100) surface only. Table 1 gives coordination numbers and adsorption energies for the six surfaces studied herein, the Supporting Information Figure S25 contains the corresponding plot. Adding our data to previous analysis [20], it is unclear if a correlation indeed exists. In particular, methoxy on the pristine (100) surface and over a vacancy in the (100) surface is coordinated to two cerium atoms but the dissociative adsorption energy differs by about 1 eV. Also, the hypothesis that the reactivity of surfaces towards oxidative dehydrogenation correlates with oxygen defect formation energies [52] was reiterated for activation energies of methoxy C-H cleavage on ceria (111) and (100) surfaces [20]. Although our surface cell is too small for a quantitative determination of vacancy formation energies, the trend we find for ceria surfaces is (111) [3.1 eV] > (100) [2.6 eV] > (110) [2.3 eV]. The same trend has been found previously [53] and does not correlate well with the barriers for C-H cleavage on the pristine surfaces, see Table 1.

While dehydrogenation on the pristine surfaces is thermoneutral or exothermic, it is endothermic over a vacancy. This suggests that the methoxy oxygen is more effective in replacing the formally double negatively charged lattice oxygen than the formaldehyde oxygen, which is consistent with the assignment of a negative charge to surface methoxy that is concentrated on the oxygen atom [39]. For all surfaces studied herein, C-H cleavage leads to a meta-stable product, where the oxygen in formaldehyde binds to the surface. This potentially opens a desorption channel. However, monodentate formaldehyde converts to a bidentate species (dioxymethylene) without barrier or a barrier smaller than 0.2 eV in all cases. The Supporting Information S1-S21 contains the NEB paths for all transition state searches for C-H cleavage and for formaldehyde conversion from monodentate to bidentate. In dioxymethylene, the carbon atom in formaldehyde binds

to a surface oxygen, which results in a considerably more stable surface species compared to monodentate formaldehyde. As a consequence, we expect the amount of monodentate formaldehyde on the surface to be extremely small.

Stabilization due to an additional bond between carbon in formaldehyde and a surface oxygen is similar on the pristine surface and over a vacancy on the (100) and (110) surfaces as can be seen in Figures 3 and 4. On the (111) surface (see Figure 2), there is less energy gain over a vacancy than on the pristine surface when the bidentate species is formed. This is likely due to the significant displacement off the lattice position of the surface oxygen that undergoes bonding when formaldehyde is located in the vacancy. The formaldehyde structures are depicted in Figure 5. On the pristine surfaces, little lattice response accompanies creation of the additional carbon-oxygen bond. Similarly, the formation of the bidentate formaldehyde species on the defective (100) surface requires only a small displacement of the surface oxygen. In addition, relocation of oxygen atoms is expected to be energetically less demanding on the (100) surface than on the the other two surfaces due to the removal of 50% of oxygen atoms in the pristine top layer. Over a vacancy on the (110) surface, we observe a significant displacement of the lattice oxygen despite the similar energy gain over a vacancy and on the pristine (110) surface when the dioxymethylene species is formed. Lattice distortion of the defective (110) surface might occur with a comparable energy penalty than the proximity of the CH_2 group to surface cerium atoms on the pristine (110) surface, see discussion below. Note the small energy difference between monodentate and bidentate species on both (110) surfaces. Also note, that on the (110) surface, surface hydrogen atoms are located within the top layer; i.e. in the same plane as the surface oxygen and cerium atoms; forming hydrogen bonds with neighboring surface oxygen atoms. This makes an alternative bidentate species (hydroxyoxymethylene) available on the pristine surface as well as over a vacancy, where the carbon oxygen bond is formed with a surface oxygen that is bound to hydrogen. This structure was given as the bidentate product in reference[19] on the pristine surface. However, the dioxymethylene structures shown in Figure 5 are lower in energy than the hydroxyoxymethylene species and form with virtually no barrier from the monodentate species, see Supporting Information S15, S19.

Included in Table 1 are experimental desorption energies derived from TPD data[7] as described in the computational details. For the (111) surface, comparison of desorption energies to experimental values suggests that the position of the desorption peak of formaldehyde is controlled by the desorption energy of the bidentate species. However, the entropic contribution to the desorption process is -0.3 eV at 600 K calculated with a recently derived formula[46] and a gas phase entropy of 218.95 $JK^{-1}mol^{-1}$ [47]. Taking the entropic contribution into account, our data indicates that formaldehyde desorbs after formation on the pristine (111) surface, indeed no further reaction products are observed in the TPD spectrum. Over a vacancy on the (111) surface and on the pristine (100) surface desorption of formaldehyde may occur but the desorption energy is high enough for bidentate formaldehyde to remain on the surface for further reaction, explaining the occurrence of carbon oxides in the TPD spectra for reduced (111) and pristine (100) surfaces. This is in agreement with prior work[20]. However, little or no formaldehyde was detected on the reduced (100) surface compared to carbon monoxide. We computed a desorption energy of 2.74 eV (~2.44 eV including the entropic term) for dioxymethylene over a vacancy on the reduced (100) surface, which makes the occurrence of further reactions before desorption probable. For the (110) surface, the desorption energies are smaller and we expect the desorption temperature to be determined by the activation energy of formaldehyde formation. Similarly to the pristine (111) surface, we predict that formaldehyde is the dominant product over carbon monoxide in a TPD experiment on the oxidized and likely a competitive product on the defective (110) surface. However, for the pristine (111) surface, a single formaldehyde desorption peak is counter-intuitive adopting our current hypothesis that low temperature water desorption, which is observed in excess on the pristine (111) surface only[7], stabilizes atop methoxy and produces methoxy in a vacancy site[39], which should lead to a second, higher temperature desorption peak. A detailed kinetic study is under way to resolve this among others. Also, the computed desorption energy for formaldehyde appears underestimated on the pristine (111) surface.

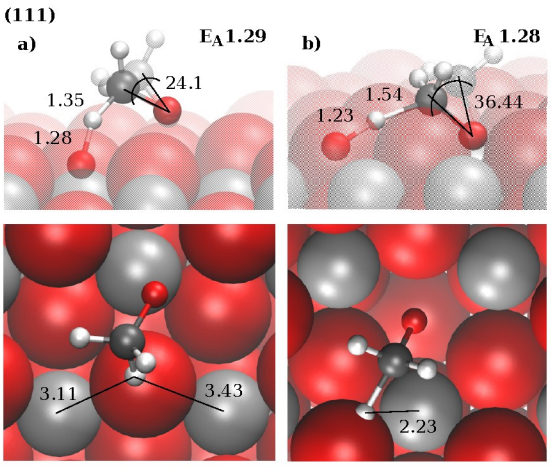

Fig. 6 Side (upper) and top (lower) view of the transition states (opaque) for C-H cleavage on the (111) ceria surface (transparent); top panel also shows methoxy (transparent); a) pristine surface, b) adsorbate over vacancy; C-H, O-H, and Ce-H distances in Å, tilting angle of O-C axis in transition state relative to methoxy in °, activation energies in eV; crystal radii[48] used for rendering of the surface atoms; red - oxygen, silver - cerium, gray - carbon, white - hydrogen.

The barrier for abstraction of a hydrogen atom in methoxy by a surface oxygen on the (111) surface does not depend on the degree of surface reduction, see Table 1. This is in agreement with prior work[16], where a barrier difference below 0.1 eV was calculated for the pristine and reduced (111) surface. While activation energies for C-H cleavage on the (100) and (110) surfaces are similar as well, we observe larger variations. To gain insight into the correlation between structural parameters, degree of surface reduction, and barriers for methoxy dehydrogenation, we explore alternative pathways, where hydrogen is transferred to different surface oxygens. Side and top views of the transition

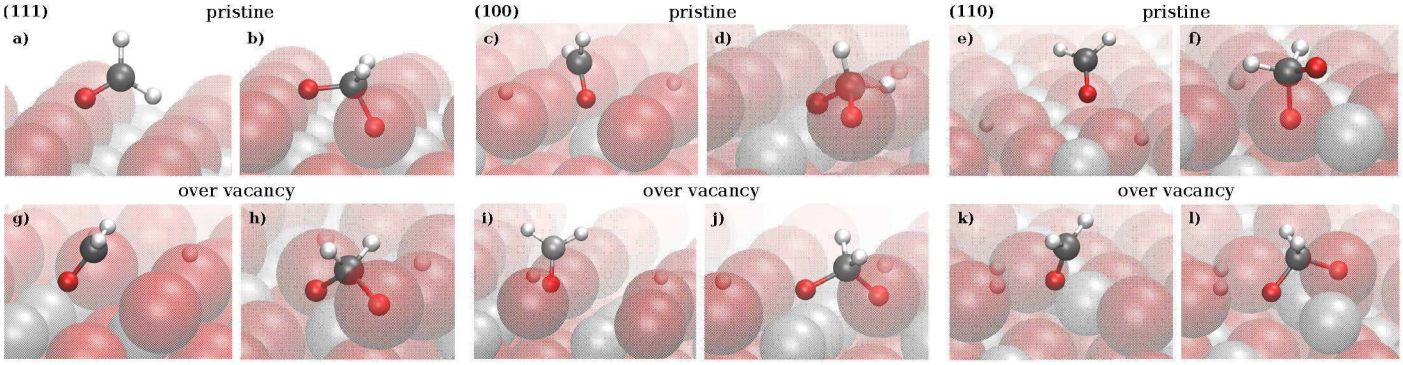

Fig. 5 Side view of formaldehyde (opaque) on ceria surfaces (transparent); a) monodentate pristine (111), b) bidentate pristine (111), c) monodentate pristine (100), d) bidentate pristine (100), e) monodentate pristine (110), f) bidentate pristine (110), g) monodentate (111) over vacancy, h) bidentate (111) over vacancy, i) monodentate (100) over vacancy, j) bidentate (100) over vacancy, k) monodentate (110) over vacancy, l) bidentate (110) over vacancy; crystal radii[48] used for rendering of the surface atoms; red - oxygen, silver - cerium, white - hydrogen, gray - carbon.

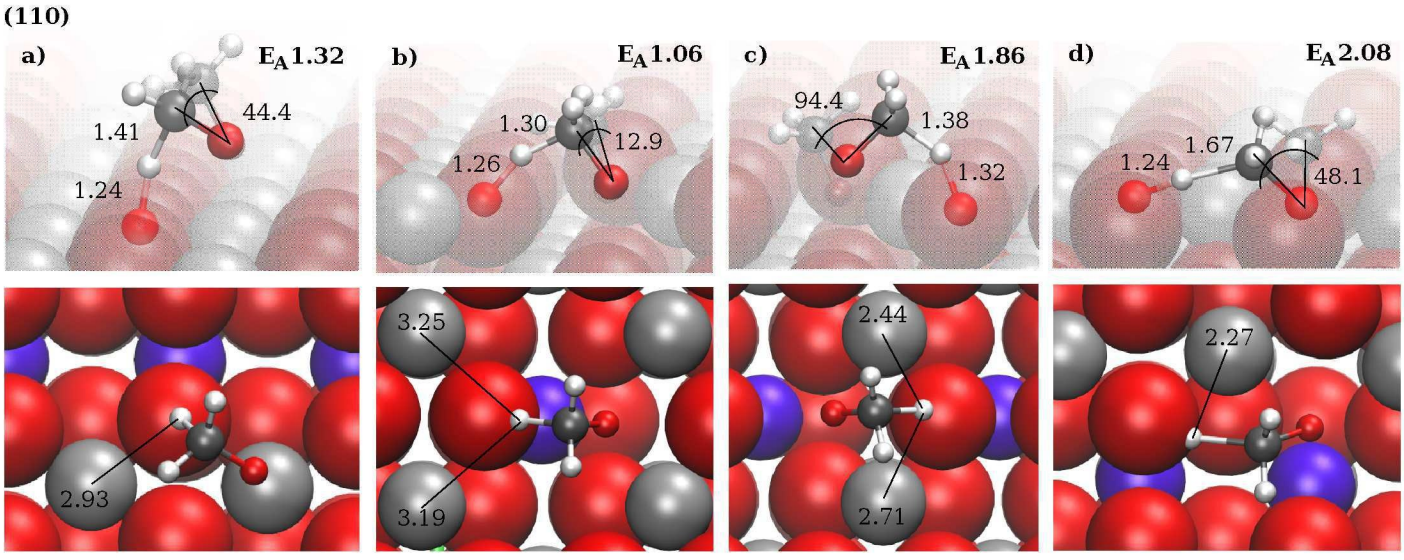

Fig. 8 Side (upper) and top (lower) view of the transition states (opaque) for C-H cleavage on the (110) ceria surface (transparent); top panel also shows methoxy (transparent); a) oxidized surface, b)-d) adsorbate over vacancy with H transfer to b) neighboring surface oxygen closest to methoxy and not hindered by Ce, c) neighboring surface oxygen closest to methoxy and hindered by Ce, d) neighboring surface oxygen furthest from methoxy; C-H, O-H, and Ce-H distances in Å, tilting angle of O-C axis in transition state relative to methoxy in °, activation energies in eV; crystal radii[48] used for rendering of the surface atoms; red - oxygen, purple - cerium (general), silver - cerium top layer, gray - carbon, white - hydrogen.

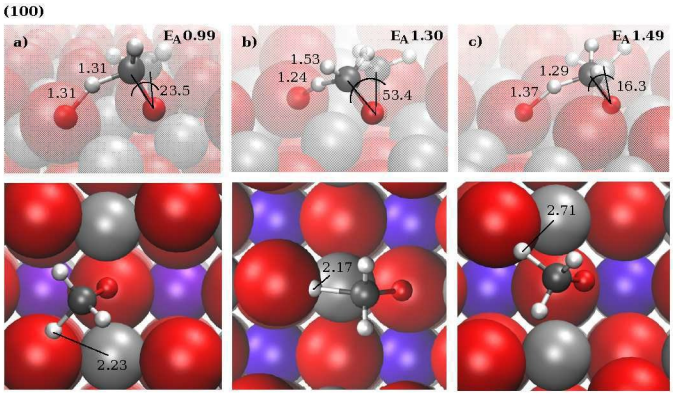

Fig. 7 Side (upper) and top (lower) view of the transition states (opaque) for C-H cleavage on the (100) ceria surface (transparent); top panel also shows methoxy (transparent); a) oxidized surface, b) adsorbate over vacancy, c) adsorbate next to vacancy; C-H, O-H, and Ce-H distances in Å, tilting angle of O-C axis in transition state relative to methoxy in °, activation energies in eV; crystal radii[48] used for rendering of the surface atoms; red - oxygen, purple - cerium (general), silver - cerium second layer, gray - carbon, white - hydrogen.

state structures together with selected structural parameters corresponding to the energy profiles in Figures 2-4 and to the pathways discussed below can be found in Figures 6-8. Activation energies for C-H cleavage are included in the figures as well. For the (111) surface, the surface oxygen atoms that neighbor methoxy on the pristine surface as well as over a vacancy are equivalent and no additional paths were examined. On the pristine (100) and over a vacancy on the (100) surface, methoxy hydrogen can be transferred to an oxygen neighboring surface hydrogen (from O-H cleavage in methanol) or to an oxygen without hydrogen neighbors. Since the oxygen atoms are otherwise equivalent, we expect the difference between these pathways to be small, which is confirmed by the energy profiles for the pristine (100) surface in the Supporting Information S22. We do not further investigate the influence of the location of the coadsorbed hydrogen.

The (100) surface is distinct from the other two surfaces through the large interatomic distances between the oxygen atoms of the top layer. If methoxy is located in a vacancy, there are empty oxygen sites available next to the vacancy, labelled N in Figure 1. Methoxy can move without barrier between the vacancy site and the sites next to it, see Supporting Information S9. The vacancy site is thermodynamically slightly preferred by 0.25 eV. The energy profiles comparing the two sites with respect to formaldehyde formation are given in the Supporting Information S23. While the C-H cleavage barrier is slightly lower for methoxy in the vacancy than in the empty oxygen site next to it, the energy profiles are similar. In Figures 6-8, we list distances between the transferred hydrogen and the surface oxygen, methoxy carbon, and first or second layer cerium atoms. The hydrogen cerium interaction is expected to be repulsive. As a measure for how large the deviation of the methoxy position in the transition state from its optimal position is, we also include the tilting angle of the C-O axis in the transition state relative to methoxy. While the barrier for C-H cleavage on the pristine (100) surface is smaller than on both (111) surfaces and on the defective (100) surface, we cannot find a structural indicator for the lower barrier, the surface oxygen site appears to be similarly available on these surfaces.

On the pristine (110) surface, the oxygen atoms neighbouring methoxy are equidistant from the Ce^{4+} adsorption site. On the defective (110) surface, the oxygen atom that partially occupies two lattice oxygen positions in the (110) vacancy structure of Figure 1 is pushed back to its original lattice location and methoxy oxygen resides at the vacancy site. This results in three different oxygen atoms that neighbor methoxy and to which hydrogen can be transferred to, two are close but not equivalent and one oxygen is further away. The energy profiles corresponding to the three hydrogen transfer pathways for methoxy over a vacancy on the (110) surface are given in the Supporting Information S24. The transition states for each pathway for C-H cleavage on the pristine and defective surface are depicted in Figure 8 together with the activation energies. For the (110) surface, we observe that the barrier increases with decreasing distance of the transferred hydrogen to the surrounding cerium atoms. This might be more pronounced on the (110) surface than on the (111) and (100) surfaces because the cerium atoms on the (110) surface are located in the top layer, where their charges are not screened by oxygen atoms in the layer above. The effect of the cerium atom proximity on the activation barrier can most clearly be seen when comparing the transition states in Figures 8 b) and c). The oxygen atoms to which hydrogen is transferred to are similarly accessible. However, the transferred hydrogen in Figure 8 c) is close to two surface cerium atoms while the closest cerium atoms in Figure 8 b) are behind the oxygen atom with reference to the transferred hydrogen. In response to the nearby cerium atoms, methoxy is pushed partly out of the vacancy in the transition state Figure 8 c). The activation barrier corresponding to transition state Figure 8 d) is also affected by the large distance between methoxy and the oxygen atom to which hydrogen is transferred to, see the elongated carbon-hydrogen bond length in Figure 8 d). On the pristine surface, we note a shorter hydrogen cerium distance and a slightly higher activation barrier than for the lowest energy transition over a vacancy.

The energy profiles for formaldehyde formation on the defective (110) surface also show that the dioxymethylene species of the lowest energy pathway is substantially less stable than for the other two pathways, see Supporting Information S24. In the transition state of the lowest pathway, Figure 8 b), the repulsion to the nearby cerium atoms is avoided but to form the bidentate species the CH_2 group has to approach the surface oxygen and experiences the same repulsion to the cerium atoms as in the transition state in Figure 8 c). Consequently, the oxygen atom of dioxymethylene that is close to the cerium atoms is partly pushed out of the surface causing a reduction in intermediate stability of more than 1.5 eV.

Although hydrogen is abstracted by a basic oxygen site during methoxy dehydrogenation, it is difficult to relate oxygen basicity and barrier height. Figure 9 shows the projected density of states (PDOS) for a surface oxygen compared to a bulk-like oxygen in the 4th layer for the different surfaces. The largest shift towards the Fermi level of the oxygen p-states is observed for the (100) surface. This can be explained by the degree of undercoordina-

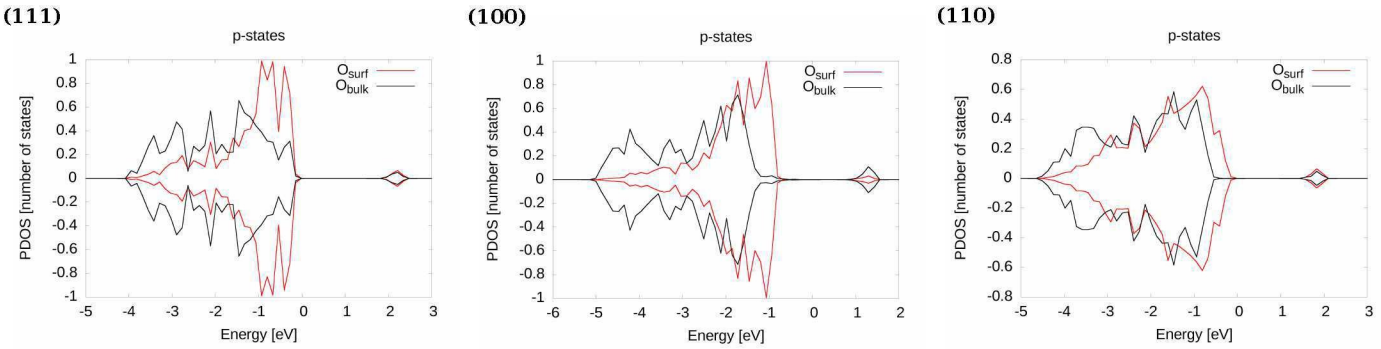

Fig. 9 Projected density of states as a function of energy per unit cell and atom for the highest occupied p-band of a surface oxygen (surf) and a 4th layer oxygen (bulk) compared for the (111), (100), and (110) surfaces.

tion of the surface oxygen. On the (111) and the (110) surfaces, the surface oxygen is coordinated with three, while on the (100) surface with two cerium atoms instead of four in the bulk. Similarly, when methoxy is adsorbed on the pristine and defective surfaces, the PDOS for the p-states of the oxygen atom to which hydrogen is transferred to show the most pronounced shift towards the Fermi level for the (100) surfaces, see Supporting Information S26-S28. If we assume that a larger shift of the oxygen p-states towards the Fermi level corresponds to higher basicity, which should aid hydrogen abstraction, then the low barrier for C-H cleavage on the pristine (100) surface is plausible. However, it does not explain the low barrier over a vacancy on the (110) surface.

4 Conclusions

We have used DFT+U to study dehydrogenation of methoxy on pristine and defective (111), (100), and (110) ceria surfaces. On all investigated surfaces, dehydrogenation leads to a metastable monodentate formaldehyde species that converts with little or no barrier (< 0.2 eV) to a bidentate species. Energy profiles are very similar. In particular, activation barriers for carbon-hydrogen cleavage are within a narrow range of 0.99 - 1.32 eV. However, intermediate stabilities differ for the different surfaces. Our data indicate that varying product distributions observed in TPD spectra of methanol conversion over ceria surfaces[7] are the consequence of the interplay between barrier controlled carbon-hydrogen cleavage and the energy requirements for formaldehyde desorption. A correlation between structural or electronic parameters and computed activation energies for carbon-hydrogen cleavage on all surfaces was not found. Although the energy differences may be too subtle for interpretation, surface oxygen basicity might influence the barrier height for hydrogen transfer. On the (110) surface, proximity of the transferred hydrogen to surface cerium atoms plays a role. A previously determined correlation between vacancy formation energies and activation energies for the different surfaces[20] is not supported by our data.

Acknowledgements

This research was sponsored by the Division of Chemical Sciences, Geosciences, and Biosciences, Office of Basic Energy Sciences, U.S. Department of Energy. The computational part of this project was conducted at the Center for Nanophase Materials Sciences under a user proposal. The Center is sponsored at Oak Ridge National Laboratory by the Scientific User Facilities Division, Office of Basic Energy Sciences, U.S. Department of Energy. This research was in part supported by an allocation of advanced computing resources provided by the National Science Foundation and performed on Kraken and Darter at the National Institute for Computational Sciences (http://www.nics.tennessee.edu/). This research also used resources of the National Energy Research Scientific Computing Center, a DOE Office of Science User Facility supported by the Office of Science of the U.S. Department of Energy under Contract No. DE-AC02-05CH11231.

References

1 *Catalysis by Ceria and Related Materials*, ed. A. Trovarelli and P. Fornasiero, Imperial College Press: London, 2nd edn, 2013, vol. 12.
2 R. J. Gorte, *AICHE*, 2010, **56**, 1126 – 1135.
3 H.-Y. Chen and H.-L. Chang, *Johnson Matthey Technol. Rev.*, 2015, **59**, 64 – 67.
4 S. S. Lee, W. Song, M. Cho, H. L. Puppala, P. Nguyen, H. Zhu, L. Segatori, and V. L. Colvin, *ACS Nano*, 2013, **7**, 9693 – 9703.
5 R. A. Yokel, M. T. Tseng, M. Dan, J. M. Unrine, U. M. Graham, P. Wu and E. A. Grulke, *Nanomed-Nanotechnol*, 2013, **9**, year.
6 Q. Yuan, H. H. Duan, L. L. Li, L. D. Sun, Y. W. Zhang and C. H. Yan, *J. Colloid Interface Sci.*, 2009, **335**, 151 – 167.
7 D. R. Mullins, P. M. Albrecht and F. C. Calaza, *Top. Catal.*, 2013, **56**, 1345 – 1362.
8 D. Mullins, *Surf. Sci. Rep.*, 2015, **70**, 42 – 85.
9 M. Li, Z. Wu and S. H. Overbury, *J. Cat.*, 2013, **306**, 164 – 176.
10 A. K. P. Mann, Z. L. Wu and S. H. Overbury, in *Catalysis by Materials with Well-Defined Structures*, ed. Z. Wu and S. H. Overbury, Elsevier, 2015, ch. The Characterization and Structure-Dependent Catalysis of Ceria with Well-Defined Facets, pp. 71 – 97.
11 Z. L. Wu, M. J. Li, D. R. Mullins and S. H. Overbury, *ACS Catalysis*, 2012, **2**, 2224 – 2234.
12 D. Kulkarni and I. E. Wachs, *Appl. Catal. A: General*, 2002,

237, 121 – 137.
13 D. R. Mullins, S. D. Senanayake and T.-L. Chen, *J. Phys. Chem. C*, 2010, **114**, 17112 – 17119.
14 D. Mei, N. A. Deskins, M. Dupuis and Q. Ge, *J. Phys. Chem. C*, 2007, **111**, 10514 – 10522.
15 A. Beste, D. R. Mullins, S. H. Overbury and R. J. Harrison, *Surface Science*, 2008, **602**, 162 – 175.
16 T. Kropp and J. Paier, *J. Phys. Chem. C*, 2014, **118**, 23690 – 23700.
17 D. R. Mullins, M. D. Robbins and J. Zhou, *Surface Science*, 2006, **600**, 1547 –1558.
18 P. M. Albrecht and D. R. Mullins, *Langmuir*, 2013, **29**, 4559 – 4567.
19 M. Capdevila-Cortada, M. García-Melchor and N. López, *J. Cat.*, 2015, **327**, 58 – 64.
20 T. Kropp and J. Paier, *J. Phys. Chem. C*, 2015, **119**, 23021 – 23031.
21 D. Mei, N. A. Deskins, M. Dupuis and Q. Ge, *J. Phys. Chem. C*, 2008, **112**, 4257 – 4266.
22 T. Kropp, J. Paier and J. Sauer, *J. Am. Chem. Soc.*, 2014, **136**, 14616 – 14625.
23 D. Mei, N. A. Deskins and M. Dupuis, *Surface Science*, 2007, **601**, 4993 – 5001.
24 B.-T. Teng, S.-Y. Jiang, Z.-X. Yang, M.-F. Luo and Y.-Z. Lan, *Surface Science*, 2010, **604**, 68 – 78.
25 A. Beste and S. H. Overbury, *J. Phys. Chem. C*, 2015, **119**, 2447 – 2455.
26 P. E. Blochl, *Phys. Rev. B*, 1994, **50**, 17953 – 17979.
27 G. Kresse and D. Joubert, *Phys. Rev. B*, 1999, **59**, 1758 – 1775.
28 G. Kresse and J. Hafner, *Phys. Rev. B*, 1993, **47**, 558 – 561.
29 G. Kresse and J. Hafner, *Phys. Rev. B*, 1994, **49**, 14251 – 14269.
30 G. Kresse and J. Furthmüller, *Comput. Mat. Sci.*, 1996, **6**, 15 – 50.
31 G. Kresse and J. Furthmüller, *Phys. Rev. B*, 1996, **54**, 11169 – 11186.
32 J. Paier, C. Penschke and J. Sauer, *Chem. Rev.*, 2013, **113**, 3949 – 3985.
33 J. P. Perdew, K. Burke and M. Ernzerhof, *Phys. Rev. Lett.*, 1996, **77**, 3865 – 3868.
34 S. L. Dudarev, G. A. Botton, S. Y. Savrasov, C. J. Humphreys and A. P. Sutton, *Phys. Rev. B*, 1998, **57**, 1505 – 1509.
35 M. B. Watkins, A. S. Foster and A. L. Shluger, *J. Phys. Chem. C*, 2007, **111**, 15337 – 15341.
36 M. Huang and S. Fabris, *J. Phys. Chem. C*, 2008, **112**, 8643 – 8648.
37 C. Loschen, J. Carrasco, K. M. Neyman and F. Illas, *Phys. Rev. B*, 2007, **75**, 035115–1 – 8.
38 F. C. Calaza, Y. Xu, D. R. Mullins and S. H. Overbury, *J. Am. Chem. Soc.*, 2012, **134**, 18034 – 18045.
39 A. Beste and S. H. Overbury, *Surface Science, in press*.
40 C. W. M. Castleton, J. Kullgren and K. Hermansson, *J. Chem. Phys.*, 2007, **127**, 244704–1 – 11.
41 N. V. Skorodumova, M. Baudin and K. Hermansson, *Phys. Rev. B*, 2004, **69**, 075401–1 – 8.
42 J. E. Sutton, A. Beste and S. H. Overbury, *Phys. Rev. B*, 2015, **92**, year.
43 M. Nolan, *Chem. Phys. Lett.*, 2010, **499**, 126 – 130.
44 J. Kullgren, K. Hermansson and C. Castleton, *J. Chem. Phys.*, 2012, **137**, 044705–1 – 044705–9.
45 P. A. Redhead, *Vacuum*, 1962, **12**, 203 – 211.
46 C. T. Campbell and J. R. V. Sellers, *J. Am. Chem. Soc.*, 2012, **134**, 18109 – 18115.
47 http://webbook.nist.gov.
48 R. D. Shannon, *Acta Cryst*, 1976, **A32**, 751 âĂŞ 767.
49 S. Grimme, J. Antony, S. Ehrlich and H. Krieg, *J. Chem. Phys.*, 2010, **132**, 154104–1 – 154104–19.
50 H. Jónsson, G. Mills and K. W. Jacobsen, in *Classical and Quantum Dynamics in Condensed Phase Simulations*, ed. B. J. Berne, G. Ciccotti and D. F. Coker, World Scientific, New Jersey, 1998, ch. Nudged Elastic Band Method for Finding Minimum Energy Paths of Transitions, p. 385.
51 G. Henkelman, B. P. Uberuaga and H. Jónsson, *J. Chem. Phys.*, 2000, **113**, 9901 – 9904.
52 J. Sauer and J. Döbler, *Dalton Trans.*, 2004, 3116 – 3121.
53 M. Nolan, S. C. Parker and G. W. Watson, *Surface Science*, 2005, **595**, 223 – 332.
54 *Model Systems in Catalysis Single Crystals to Supported Enzyme Mimics*, ed. R. M. Rioux, Springer, 2010.